Polymer 49 (2008) 3805–3815

Contents lists available at ScienceDirect

Polymer

journal homepage: www.elsevier.com/locate/polymer

Highly dispersed nanosilica–epoxy resins with enhanced mechanical properties

Chenggang Chen [a], Ryan S. Justice [b,c], Dale W. Schaefer [c], Jeffery W. Baur [b,*]

[a] University of Dayton Research Institute, 300 College Park, Dayton, OH 45469-0060, United States
[b] Air Force Research Laboratory, Materials and Manufacturing Directorate, WPAFB, OH 45433-7750, United States
[c] University of Cincinnati, Department of Chemical and Materials Engineering, Cincinnati, OH 45221-0012, United States

ARTICLE INFO

Article history:
Received 23 January 2008
Received in revised form 8 June 2008
Accepted 9 June 2008
Available online 18 June 2008

Keywords:
Nanocomposites
Small-angle scattering
Mechanical properties

ABSTRACT

Epoxy–nanocomposite resins filled with 12-nm spherical silica particles were investigated for their thermal and mechanical properties as a function of silica loading. The nanoparticles were easily dispersed with minimal aggregation for loadings up to 25 wt% as determined using transmission electron microscopy (TEM) and ultra-small-angle X-ray scattering (USAXS). A proportional decrease in cure temperatures and glass transition temperature (for loadings of 10 wt% and above) was observed with increased silica loading. The morphology determined by USAXS is consistent with a zone around the silica particles from which neighboring particles are excluded. The "exclusion zone" extends to 10× the particle diameter. For samples with loadings less than 10 wt%, increases of 25% in tensile modulus and 30% in fracture toughness were obtained. More highly loaded samples continued to increase in modulus, but decreased in strength and fracture toughness. Overall, the addition of nanosilica is shown as a promising method for property enhancement of aerospace epoxy composite resins.

Published by Elsevier Ltd.

1. Introduction

Because of their superior properties and low cost, epoxy resins are widely used in adhesives, coatings, electronic encapsulants, medical devices, optical components, and structural composites [1]. However, the brittle nature of most high-performance epoxy resins necessitates the incorporation of toughening agents. Numerous toughening strategies have been explored including incorporation of rubber particles, core–shell particles, glass beads, microvoids, hyperbranched polymers, thermoplastic particles, inorganic particles, as well as combinations of these materials [2].

Toughness is enhanced by increasing the fracture energy through a variety of energy-dissipative mechanisms. The mechanism is dependent on a number of variables including the nature of the inclusion, the inclusion size, and loading. In the case of toughening with micron-sized rubber particles, energy is dissipated in the plastic zone near the crack tip through yielding processes such as void formation [3], shear flow [4,5], and matrix stretching [6]. Unfortunately, low modulus rubber particles typically decrease the modulus and thermal properties of the resin system. Contrastingly, thermoplastic-particle-reinforced epoxies show minimal decrease in modulus and thermal properties. Toughening is also achieved via delocalized cracking and crack-bridging [7]. Toughening with high-modulus, micron-sized particles has been shown to occur via many different mechanisms of energy dissipation without compromising the modulus or thermal properties of the composite. Examples of such mechanisms include crack trapping and bridging [8], crack-path deflection [9], microcracking [10], particle debonding, void formation, and yielding of the interparticle matrix [11].

Recently, new strategies have appeared utilizing nanoparticles to improve toughness and other mechanical properties [12]. Several studies indicate that modulus, strength, and toughness can be simultaneously increased with the addition of nano-scale fillers [2,12–18]. The proposed toughening mechanisms include enhancement of the energy for crack propagation by increasing the number of hard-particle interactions [19] or by altering the properties of the polymer in proximity to the particle surface [20].

Nanoparticles can significantly alter the mechanical properties of the polymer close to the particle surface due to changes in polymer chain mobility. Enhancement in toughness has been attributed to suppression of polymer chain mobility at the nanoparticles' surface from attractive interaction revealed by an increase in glass transition temperature (T_g) and/or broadening of the dynamic mechanical loss peak [21]. Enhancement in localized chain mobility from repulsive particle interactions and/or formation of regions of enhanced free volume have been suggested to exist for some silica (SiO_2) nanoparticles and to lead to a decrease in T_g with increasing particle loading [22–25].

In the case of thermosetting polymers such as epoxies, the curing reaction can also be affected by these interactions, resulting

* Corresponding author. Air Force Research Laboratory, Materials and Manufacturing Directorate, 2941 Hobson Way, Building 654/136, WPAFB, OH 45433-7750, United States. Tel.: +1 937 255 9143; fax: +1 937 656 4706.
E-mail address: jeffery.baur@wpafb.af.mil (J.W. Baur).

0032-3861/$ – see front matter Published by Elsevier Ltd.
doi:10.1016/j.polymer.2008.06.023

in changes in cure temperature in proportion to particle loading. Reaction with particle surface groups may also affect the reaction kinetics and local stoichiometry which, in turn, leads to variations in the morphological development of the cross-linked network. Thus, the mechanical properties of a nanocomposite resin can be different from that of the matrix polymer due to variations in cross-link network formed in the presence of the nanoparticles and the local physical interactions near the particle surface [20]. Because of the larger surface-to-volume ratio of nanoparticles over traditional fillers, these effects are expected to be more prominent for a given filler volume fraction. Furthermore, since cracking and micro-mechanical deformation occur at dimensions larger than the isolated nanoparticles, it is important to understand the composite morphology at length scales larger than the size of the nanoparticles. Thus, characterization of the multi-scale morphology of dispersed nanoparticles is important to understand the properties of the nanocomposite resin [26].

Previously, Zhang and coworkers [18] investigated 25-nm diameter sol–gel SiO_2 particles in epoxy with dynamic mechanical analysis (DMA). The authors speculate that as the particle loading increases, the average interparticle distance decreased until a mechanically coupled network is formed at the critical interparticle distances. It was suggested that this network contributed to a 75% increase in toughness and a 75% increase in bending modulus when loaded up to 14 vol% [18]. In their analysis, the interphase material was assumed to be a linear-elastic material with a higher modulus than the matrix material. Rosso et al. reported a similar increase in toughness for a different epoxy system with a simultaneous increase in modulus [17]. Several researchers have also reported using SiO_2 nanoparticles in combination with micron-sized SiO_2 particles to more than double the impact toughness of a resin. These researchers proposed a mechanism involving plastic deformation and debonding around the micron-sized SiO_2 particle [13–15].

Here, we investigate the morphology, processing characteristics, and mechanical properties of nanocomposites made with colloidal SiO_2 nanoparticles ($\sim$12-nm diameter) dispersed in an aerospace epoxy matrix. To measure thermal and mechanical properties of these nanocomposites, we utilized characterization techniques such as DMA, differential scanning calorimetry (DSC), tensile testing, and impact toughness testing. In light of these measured properties, we investigated the morphology of the SiO_2 particles at various loadings using transmission electron microscopy (TEM) and ultra-small-angle X-ray scattering (USAXS). The particle diameter and the mean interparticle distance (center to center) were obtained from USAXS. Overall, this system of SiO_2 and epoxy is shown to be easily processed, thermally stable, and has simultaneous improvements in modulus and toughness at low particle loadings. At high loadings, a proportional decrease in cure temperature with loading and a significant decrease in T_g are observed with no threshold for property improvement.

2. Experimental

2.1. Materials

The composite matrix analyzed in this work is Epon 862 epoxy resin (diglycidyl ether of bisphenol F epoxy, Shell Corporation) cured with EpiCure-W (diethyl diamino toluene, Shell Corporation). Both materials were purchased from Miller-Stephenson Chemical Company, Inc. In the remainder of this work, we refer to the cured epoxy system (epoxy + cure agent) as Epon862/W. This resin system has been studied for aerospace applications due to its high working temperature, good properties, and low viscosity [27]. These properties are all significant when resin-transfer molding advanced carbon-fiber-reinforced composites.

The SiO_2 nanoparticles (MEK-ST) were purchased from Nissan Chemical as a 30-wt% suspension of SiO_2 in methyl ethyl ketone (MEK). The manufacturer specifies the average particle diameter to be 12 nm. Though it is widely accepted that the surfaces of most commercially available SiO_2 nanoparticles have been altered to enhance dispersibility, such information for MEK-ST was not available from Nissan Chemical. Consequently, the MEK-ST was analyzed by thermogravimetric analysis (TGA), Fourier transform infrared (FTIR) spectroscopy, and solid state nuclear magnetic resonance (NMR, ^{29}Si and ^{13}C). Using these analysis techniques, it was estimated that the surface organic layer represented $\sim$3 wt% of the dried nanosilicate powder. The surface consists of trimethylsilyl groups (–Si(CH_3)), short chain alkoxysilanes (possibly Si–OCH_3 and Si–OCH_2CH_3), and a small amount of hydroxyl (–OH) groups. Although a more detailed and quantitative analysis of the amount and structure of the surface groups was not performed, the data suggest that the surface has been modified to increase hydrophobicity over the native SiO_2 surface, yet the surface retains some hydrophilic and potentially reactive surface hydroxyl groups.

2.2. Sample preparation

The following protocol was followed to process the analyzed samples. The MEK-ST and Epon 862 were combined to a total mass of approximately 250 g in a 500 ml Pyrex beaker. The mixture was homogenized by simultaneously ultrasonicating (Ultrasonic Processor GEX 750 W, 50% amplitude, 20 kHz, 20% duty cycle – on for 12 s, off for 48 s) and mixing with a magnetic stir bar (3 h). The resulting mixture remained transparent even at very high loadings ($\sim$30%). The MEK from the stock SiO_2 suspension evaporated as the SiO_2/Epon 862 mixture was degassed at $\sim$75 °C and 1 torr of active vacuum in a vacuum oven. The stoichiometric amount of EpiCure-W (100:26, Epon 862:W, by weight) was then added to the SiO_2/Epon 862 mixture and homogenized using a magnetic stir bar (65 °C, 20 min). The nanocomposite resin was degassed under vacuum at $\sim$70 °C and 1 torr of active vacuum in a vacuum oven. The nanocomposites' resin was cast in either shaped silicone molds for dog-bone tensile specimens ($184 \times 19 \times 3.2$ mm in overall dimension with $64 \times 6 \times 3.2$ mm gauge section) or between glass plates for large panel samples with a thickness of 3.2 mm. The samples were cured in a conventional oven using a 30-min temperature ramp from room temperature to 121 °C and a 2 h hold, followed by a 30-min ramp from 121 to 177 °C with a 2 h hold and a slow cool to room temperature.

2.3. Characterization

Numerous characterization techniques were utilized to characterize the nanocomposites discussed in this paper. The following section details the instrumentation and sample preparation involved in the data collection.

2.3.1. Electron microscopy

Samples for TEM were microtomed in a Reichert-Jung Ultracut Microtome and mounted on 200-mesh copper grids. TEM was performed using a Philips CM200 transmission electron microscope operating at 200 kV. The fracture surface was coated with carbon and checked via SEM using a Philips XL 30 Environmental SEM.

2.3.2. Ultra-small-angle X-ray scattering

USAXS specimens used the previously mentioned 3.2 mm thick plate samples. By measuring the differential scattering cross-section as a function of the modulus of the momentum transfer wave vector (q), a scattering profile is generated. The variable q is related to the scattering angle as $q = (4\pi/\lambda)\sin(\theta/2)$, where λ is the wavelength of the X-rays and θ is the scattering angle. USAXS can resolve

q-values on the order of 10^{-4} Å$^{-1} \leq q \leq 10^{-1}$ Å^{-1} (1 Å = 0.1 nm). Therefore, USAXS is useful for elucidating morphological features in the 10,000 Å $\leq q^{-1} \leq$ 10 Å size regime.

The USAXS data were obtained at the X-ray Operations and Research beam line (32-ID-B) at the Advanced Photon Source (APS) at Argonne National Laboratory (Argonne, IL, USA). All intensity profiles are plotted on an absolute scale as the differential scattering cross-section per unit sample volume per unit detector solid angle – $d\Sigma/(Vd\Omega)$ (cm^{-1}) vs. q (Å^{-1}). Data were analyzed using Indra routines written by Jan Ilavsky at the APS.

2.3.3. Dynamic light scattering

The size of the nanosilica particles was measured in MEK using a Malvern CGS-3 Multi-Angle Light Scattering Spectrometer. The "as-received" nanosilica/MEK stock solution was diluted 500:1 in MEK by weight prior to measurement. All scattering measurements were performed at 90°, and the data were analyzed using the cumulants method [28] to determine the mean decay rate of the intensity correlation function and the second moment of the distribution of decay rates.

2.3.4. Differential scanning calorimetry

DSC was performed using a TA Instruments 2920 Differential Scanning Calorimeter ramped at 2 °C/min from room temperature to 250 °C under flowing nitrogen with a sample size of 7–10 mg.

2.3.5. Dynamic mechanical analysis

DMA was performed using a Rheometrics ARES Dynamic Spectrometer in the torsion bar geometry with a 12.7 mm × 63.5 mm × 3.2 mm rectangular specimen fabricated using the previously mentioned casting procedure. The specimens were measured at a frequency of 100 rad/s, a strain of 0.1%, and a heating rate of 2 °C/min from room temperature to 250 °C.

2.3.6. Rheological measurements

Viscosity measurements were made using the same Rheometrics ARES Dynamic Spectrometer, using a 25-mm diameter parallel-plate geometry at a frequency of 10 rad/s, a strain of 3%, and a heating rate of 2 °C/min from room temperature to 200 °C.

2.3.7. Tensile mechanical testing

The tensile test and data analysis are in accordance with the standard test method for tensile properties ASTM-D638 for plastic samples of 1 mm or greater. The overall dimensions of the samples were 184 × 19 × 3.2 mm with a 118 mm between grips and a narrow section of 64 mm in length and 3 mm in width. "Dog-bone" specimens were tested using an MTS servohydraulic test frame coupled with a TeststarIIs controller. Force control was used to load the specimens with a loading rate of 2.3 kg/s measured axially in tension to failure. Strain was monitored during the load ramp with a 2.5-mm MTS extensometer with five specimens measured for each sample.

2.3.8. Fracture toughness determination

Fracture toughness was determined using compact-tension testing in accordance with the standard test method ASTM-E399. Sample preparation included machining of a series of 19.0 mm × 19.0 mm × 3.0 mm blanks from a larger cured resin plaque described previously. The specimens were notched with an 8.9 mm × 0.3 mm slot centered between two loading pinholes. The specimens were tested using an MTS (TeststarIIs controlled) servohydraulic test frame and run in displacement control at a rate of 1.3 mm/min at room temperature. The data analysis was performed in accordance to ASTM-E399 to determine the fracture toughness, Kq.

3. Data and analysis

3.1. Processing/rheology

Fig. 1a is a TEM image of the SiO_2 from the stock suspension of MEK-ST after the MEK has been allowed to evaporate. The image indicates that the SiO_2 particles are spherical, reasonably uniform in size, and have an average diameter close to the manufacturer's reported mean value of 12 nm. While the particles look to be aggregated in the TEM, dynamic light scattering (DLS) was used to investigate if the aggregation resulted from drying the stock solution on the TEM grid. Furthermore, more quantitative information regarding the sizes of the SiO_2 particles can be determined from DLS.

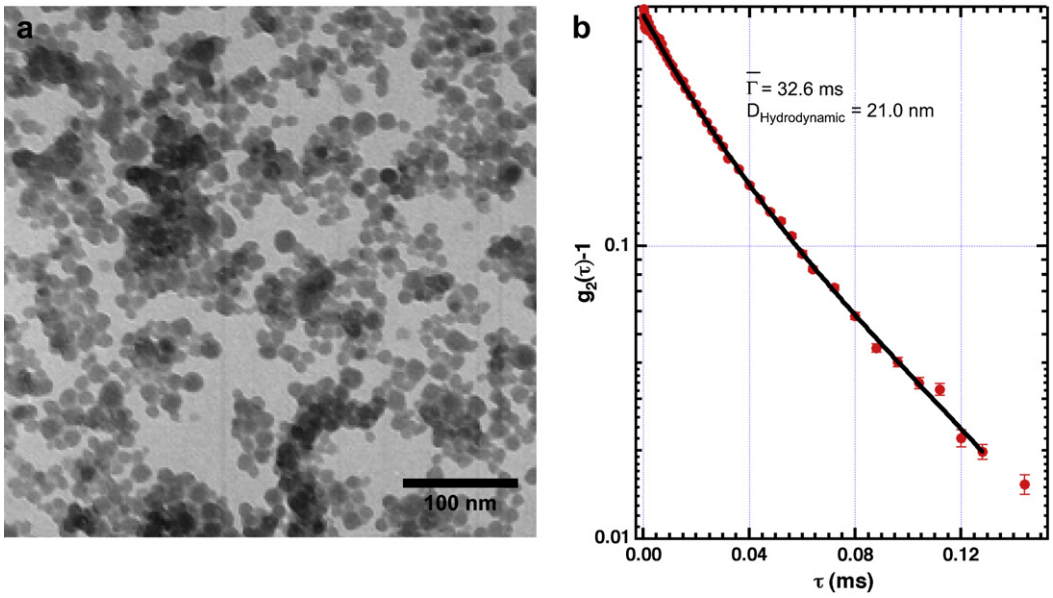

Fig. 1. TEM and dynamic light scattering of native SiO_2. (a) TEM image of the dried SiO_2 nanoparticles from the stock MEK-ST suspension. (b) Normalized intensity correlation function via dynamic light scattering of a 500:1 dilution (with MEK) of the stock MEK/SiO_2 solution (30 wt% SiO_2). The line is a third-order cumulant (polynomial) fit. The mean decay rate, $\bar{\Gamma}$, corresponds to a hydrodynamic diameter of 21.0 nm. The initial curvature corresponds to a distribution of decay time whose width is 0.64$\bar{\Gamma}$. The laser wavelength was 6328 Å and the scattering angle was 90°.

Fig. 1b shows the DLS data from a 500:1 MEK dilution (by weight) of the stock MEK-ST. The normalized (background-subtracted) intensity correlation function shown in Fig. 1b was fit to a cumulant expansion [28] to extract the mean decay rate ($\overline{\Gamma} = \langle\Gamma\rangle$) and the normalized width of the decay-rate distribution $(\langle(\Gamma - \overline{\Gamma})^2\rangle\overline{\Gamma}^{-2})^{1/2}$. The observed mean decay rate of 32.6 ms at scattering angle of 90° corresponds to a mean hydrodynamic diameter of 21.0 nm using the Stokes–Einstein relationship. The larger measured diameter (compared to the manufacturer's value of 12 nm) and the observed normalized width of 0.64 are consistent with the presence of some aggregation of the SiO_2 particles in the stock solution.

Due to their small size and low aspect ratio, the SiO_2 nanoparticles are expected to only slightly increase the resin viscosity. Rheological measurements on the uncured resin for loadings up to 10 wt% as a function of temperature (Fig. 2) confirm a low viscosity, thus a large processing window exists prior to the initiation of cure. As loading increases, the curing response shifts to lower temperature. The onset temperature is taken from the crossing of tangent lines representing the minimum viscosities and the trend at the steepest part of the curves (tangent lines not shown). The maximum cure temperature was taken as the maximum of the derivative of the viscosity profile. The decrease in maximum cure temperature of the bulk as measured by viscosity is linearly proportional to the amount of SiO_2 added with an average decrease of 1.2 °C/wt% SiO_2.

The DSC data in Fig. 3, which compares the normalized heat flow as a function of temperature, also confirm the lower temperature cure of the epoxy in the presence of the nanosilica. While the total heat of reaction does not change with loading, a significant decrease in the onset temperature (−2.8 °C/wt% SiO_2) and maximum heat flow (−1.6 °C/wt% SiO_2) is observed as the reaction peak is broadened.

DMA was used to investigate the effects of filler loading on the T_g of the cured Epon862/W samples. Fig. 4 presents the tan δ vs. temperature data for Epon862/W with loadings between 0.0 and 20.0 wt% SiO_2. From the tan δ curves, the first deviation from the unfilled Epon862/W T_g occurs in the 10 wt% sample followed by a linear suppression of T_g at a rate −3.8 °C/wt% SiO_2.

3.2. Morphology

Fig. 5a shows TEM images of a cured SiO_2/Epon862/W composite at 1.3 wt% loading. SiO_2 is well dispersed with minimal aggregation. Individual nanoparticles ranging in diameter from ~12 to 20 nm closely resemble the individual SiO_2 particles (non-aggregated) visible in the TEM of the dry powder shown in Fig. 1a. Additionally, Fig. 5b and c compares TEM images of nanocomposites loaded at 5 and 15 wt%. The SiO_2 particles show minimal signs of aggregation, consistent with the retention of optical transparency at the higher loadings.

To quantify the level of aggregation and overall SiO_2 morphology, USAXS was measured as a function of filler loading. The scattering profiles after subtraction of a pure epoxy background (0-wt% SiO_2) are shown in Fig. 6. These profiles provide information about both the morphology of the particles and the correlations among particles.

The USAXS data in Fig. 6 are characteristic of a correlated system of particles. There is no evidence for large-scale aggregation, which would produce intense scattering at small q. For a dilute system of non-correlated particles, the scattering intensity is given by

$$I(q) = \phi v\left(\Delta\rho^2\right)F(q)^2 \quad (1)$$

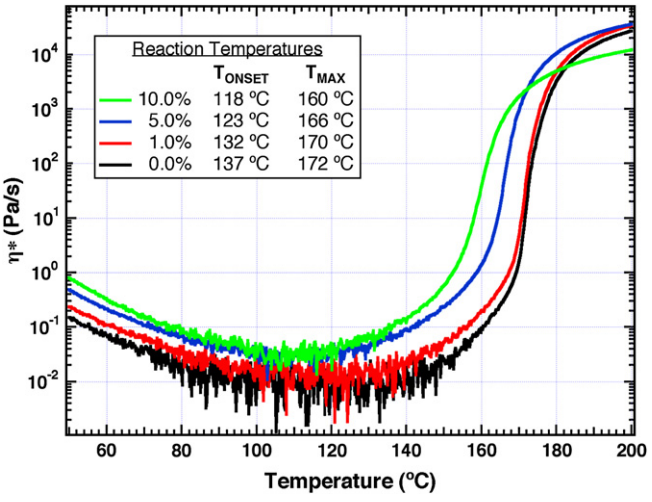

Fig. 2. Viscosity vs. temperature data from a series of SiO_2/Epon862/W nanocomposite samples. The onset temperature is taken from the crossing of tangent lines representing the minimum viscosities and the trend at the steepest part of the curves (tangent lines not shown). The maximum temperature was taken as the maximum of the derivative of the viscosity profile, η^*.

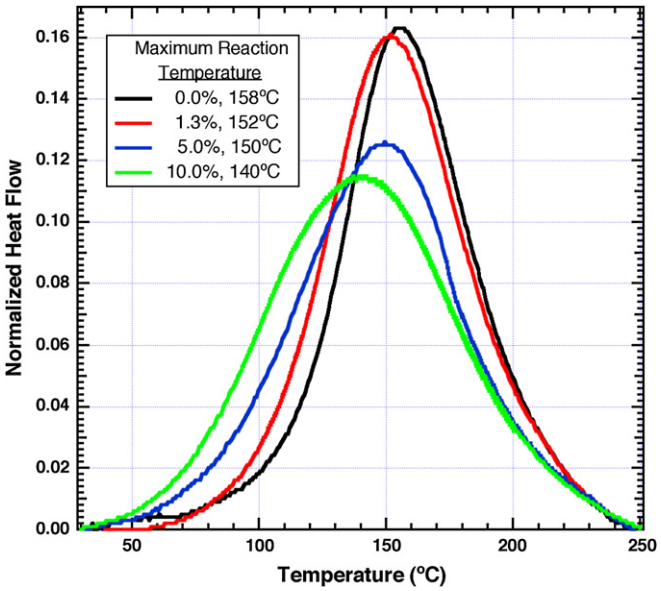

Fig. 3. The DSC data during cure of SiO_2/Epon862/W nanocomposites. The onset of polymerization decreases with loading by 2.8 °C/wt%.

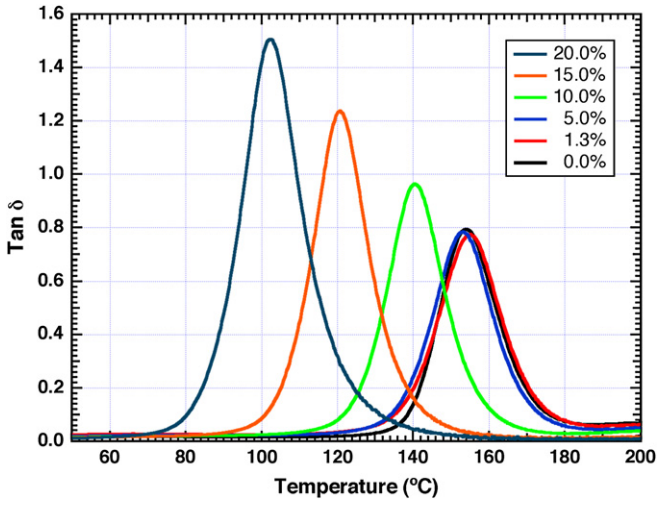

Fig. 4. The tan δ curves vs. temperature from a series of cured SiO_2/Epon862/W nanocomposite samples.

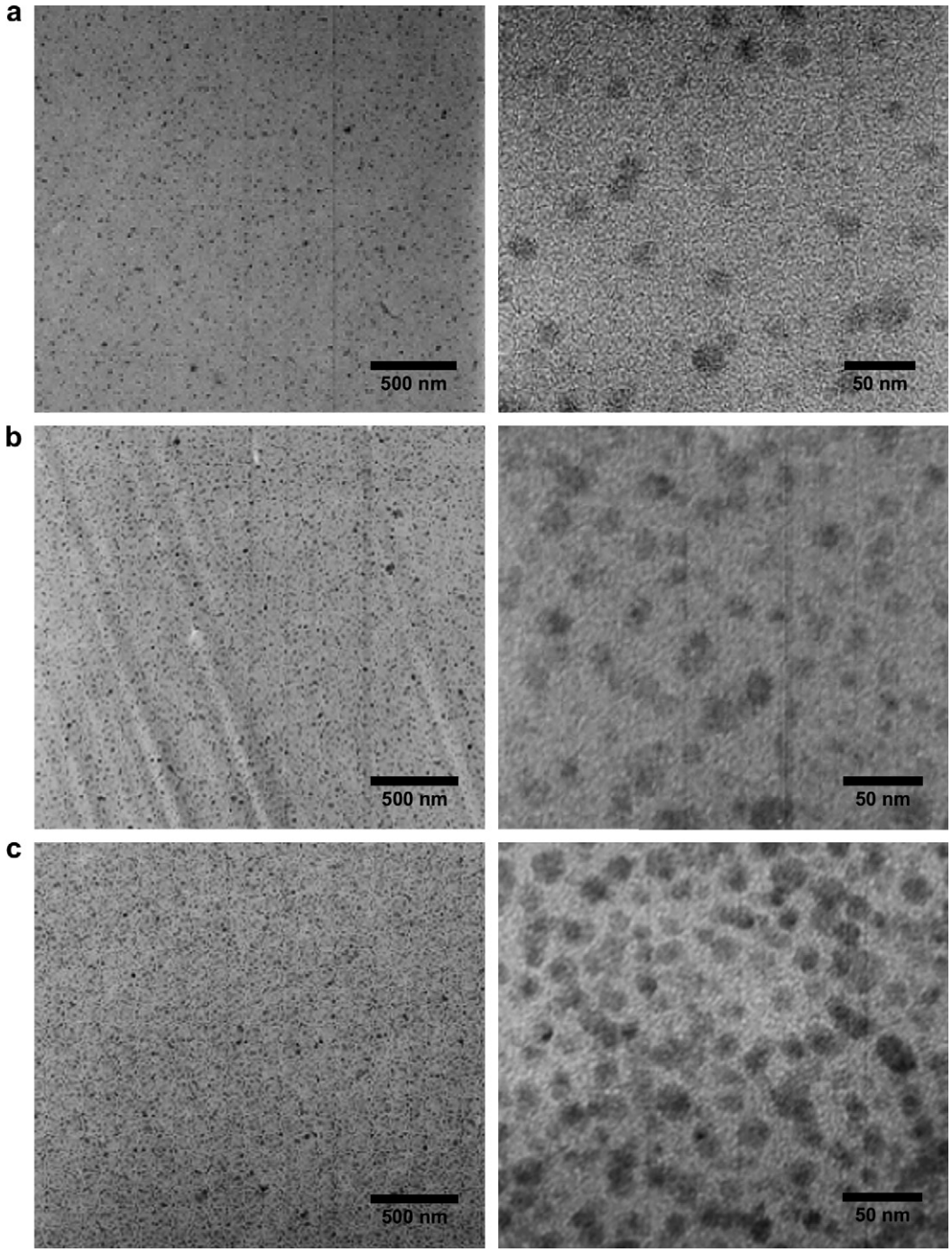

Fig. 5. TEM images of (a) 1.3-wt%, (b) 5-wt%, and (c) 15-wt% SiO_2/Epon862/W nanocomposites.

where $F(q)$ is the spherical form factor of the particles, v is the particle volume, ϕ is the volume fraction of scattering particles and $(\Delta\rho^2)$ is the contrast in scattering length density. At small q, $F(q)$ is a monotonically decreasing function of q. For a correlated system (non-random particle position distribution), the intensity is modified by a structure factor, $S(q)$, which accounts for the interparticle correlations [29]:

$$I(q) = \phi v\left(\Delta\rho^2\right)F(q)^2S(q) \tag{2}$$

In the case of randomly distributed particles, $S(q)=1$. For repulsive particles, $S(q)$ leads to a suppression of intensity at small q and a peak when q^{-1} is comparable to the interparticle distance. If the spheres interact via a hard sphere potential of range ζ [29–31],

$$S(q) = \frac{1}{1+k(g(q\zeta))}, \tag{3}$$

where

$$g(q\zeta) = \frac{3(\sin(q\zeta)-q\zeta\cos(q\zeta))}{(q\zeta)^3}. \tag{4}$$

For true hard spheres, ζ is the mean center-to-center, interparticle distance. The packing parameter (k), which describes the degree of correlation, should have the value $k=8\phi$ for true hard particles. If

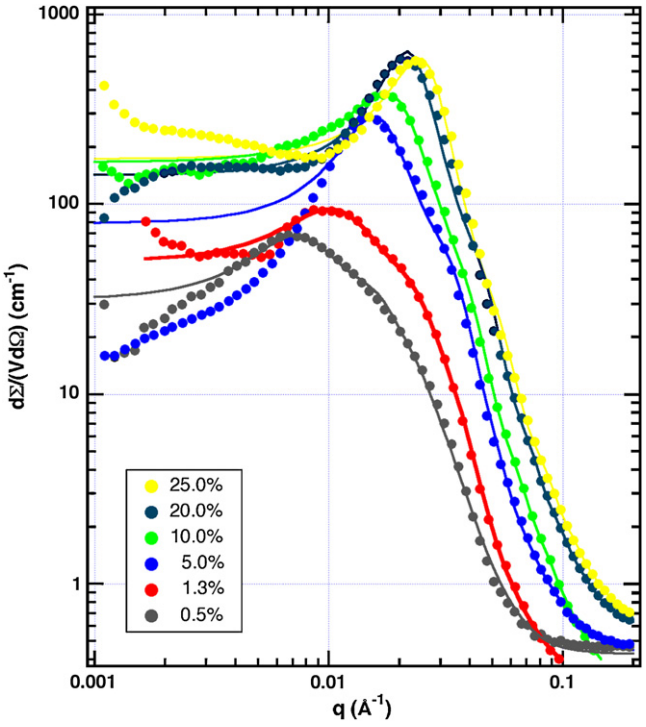

Fig. 6. Background-subtracted USAXS data for a series of SiO_2 loadings. From each scattering profile, a pure epoxy background was subtracted. The lines are fits to Eq. (2) neglecting the low-q region. The data are plotted as the differential cross-section per unit volume per unit solid angle.

the actual interparticle potential is softer than a hard sphere, we expect $k < 8\phi$. These equations are strictly valid only in the dilute limit where three-particle interactions can be ignored.

Eq. (2) was fit to the data in Fig. 6 using a so-called unified approximation to a sphere form factor [32] and the hard-sphere structure factor (Eq. (3)). Table 1 summarizes the fitting parameters calculated from the data in Fig. 6. The hard diameter, $2R$, is calculated from the Guinier radius (R_G) from the scattering profile. Except at the lowest loading, there is reasonable consistency among the sphere diameters ($2R \sim 180$–250 Å) with close proximity to the hydrodynamic diameter of 210 Å determined from DLS (Fig. 1b). The deviation from the manufacturer's value of 120 Å can be attributed to the R^6-dependence of the scattering intensity on the particle size, R. Thus a few larger (or aggregated) SiO_2 particles will cause the measured R to exceed that expected based on a number-average size. The agreement between the average diameters measured in MEK and in the cured polymer indicates that the level of dispersion of the particles in the different media is equivalent. Thus, full dispersion with mild aggregation is achieved even at high loadings.

Table 1
Calculated parameters from the unified fits of the data in Fig. 6

Loading (wt%)	Volume Fraction (ϕ)	Silica Guinier radius (R_G in Å)	Silica diameter ($2R$ in Å)	Interparticle distance (ζ in Å)	Effective vol. fraction ($\phi_{\text{eff-USAXS}}$)
0.5	0.003	97.0	250	717	0.123
1.3	0.008	79.7	205	502	0.146
5.0	0.032	75.0	193	339	0.360
10.0	0.065	77.9	201	293	0.372
20.0	0.135	69.7	179	250	0.604
25.0	0.172	67.2	174	223	0.625

The hard diameter, $2R$, is calculated from the Guinier radius (R_G) from the scattering profile. The average interparticle distance (ζ) is measured center to center. The effective volume fraction is calculated from the packing parameter, k, as $k/8$. R_G, $2R$, and ζ have the units of Å. The parameters ϕ, $\phi_{\text{eff-USAXS}}$ are unitless.

The more interesting aspect of the USAXS parameters concerns the interparticle correlations. The parameter, ζ, which quantifies the length scale over which the particles are correlated, is plotted in Fig. 7 as a function of particle volume fraction (ζ vs. ϕ). The average interparticle distance (ζ) is measured center to center with the units of Å. The parameters ϕ, $\phi_{\text{eff-USAXS}}$ are unitless.

For comparison, the mean interparticle spacing, τ, calculated assuming simple cubic packing is also shown in Fig. 7 and is given as

$$\tau = R\left(\frac{4\pi}{3\phi}\right)^{1/3} \tag{5}$$

where the best fit value of $R = 70$ Å is close to the manufacturer's reported radius of 60 Å. It is expected that ζ would track τ as observed in Fig. 7. What is unusual is that the particles are correlated at least to a volume fraction of 0.3% ($\phi = 0.003$) where the interparticle spacing is 10 times the hard-core radius.

Information on the degree of interparticle correlation is contained in the packing parameter k. The effective volume fraction can be calculated from k as

$$\phi_{\text{eff-USAXS}} = \frac{k}{8}. \tag{6}$$

The effective volume fraction would equal the actual volume fraction for true hard spheres. The effective domain size, ξ, is then

$$\xi = 2R\left(\frac{\phi_{\text{eff-USAXS}}}{\phi}\right)^{1/3}, \tag{7}$$

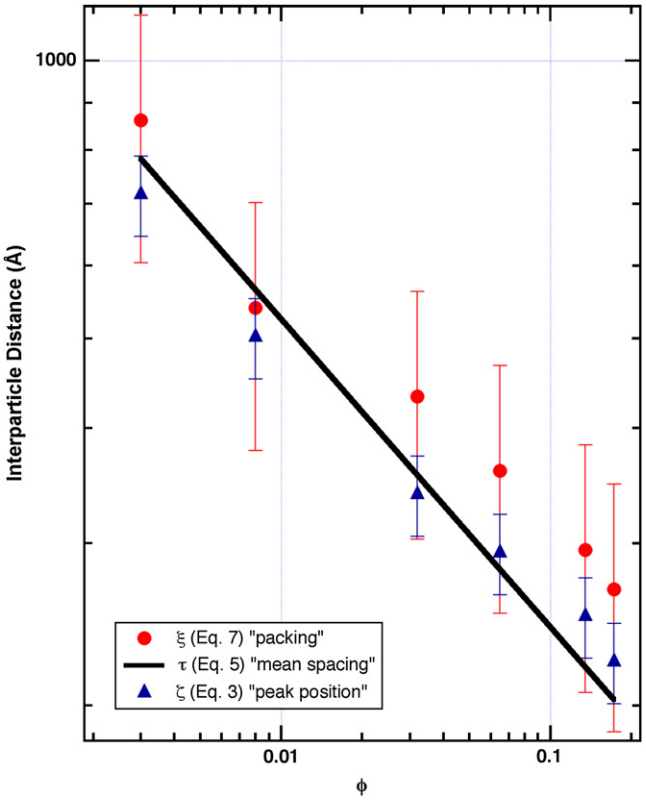

Fig. 7. Correlation range, ζ (Eq. (3)), measured by USAXS compared to the mean interparticle distance, τ, calculated from the filler loading, Eq. (5), and the effective filler domain size ξ calculated from the USAXS packing parameter (k) using Eq. (7). The fact that Eq. (7) is consistent with the measured interparticle distance at low loadings (low ϕ) testifies to the apparent repulsive nature of the interparticle interactions leading to an exclusion zone extending to 10 particle diameters.

which is also plotted in Fig. 7 with R taken from Table 1. The fact that ξ is comparable to the other measures of interparticle distance (ζ and τ) shows the silica particles, combined with the surrounding excluded volume, are behaving as quasi-hard spheres of radius much larger than the physical radius of the particles. It appears as if there is some process or repulsive interaction that is driving the SiO_2 particle to separate over length scales of up to ~750 Å. Since there are no known colloidal forces acting over this range, the highly correlated morphology must arise during processing and/or curing.

It should be noted that the above analysis ignores the data at small q in Fig. 6 where the data do not follow any trend. This region is dominated by long-range correlations, which are not considered in Eq. (2). The limited fitting region leads to the large error in ξ in Fig. 7.

3.3. Mechanical properties

The modulus and strength were measured using "dog-bone" tensile specimens. The testing shows a monotonic increase in the tensile modulus with loading up to 20 wt% along with consistent strength in the samples up to 10% (Fig. 8, Table 2). At 20 wt%, the sample was significantly more brittle with a slightly decreased strength but increased modulus. In Fig. 9, the modulus data are plotted as a modulus enhancement (E_δ = composite modulus/matrix modulus) vs. volume fraction SiO_2. The SiO_2 density is assumed to be 2.0 g/cm^3 and the matrix density is 1.25 g/cm^3. If the particles were randomly distributed, some inflection in the modulus data would be expected near $\phi = 0.16$ (the percolation threshold for hard spheres). The linear relationship, therefore, supports the USAXS conclusion regarding a non-random particle distribution.

To interpret the modulus data we use the model developed by Smallwood in 1944. Smallwood calculates E_δ assuming the filler is spherical, rigid and bonded to a rubbery (Poisson's ratio = 0.5) matrix. The elastic energy is then stored in the strain field around the particle. Smallwood proposed the intriguing result that modulus enhancement (E_δ) is independent of particle size:

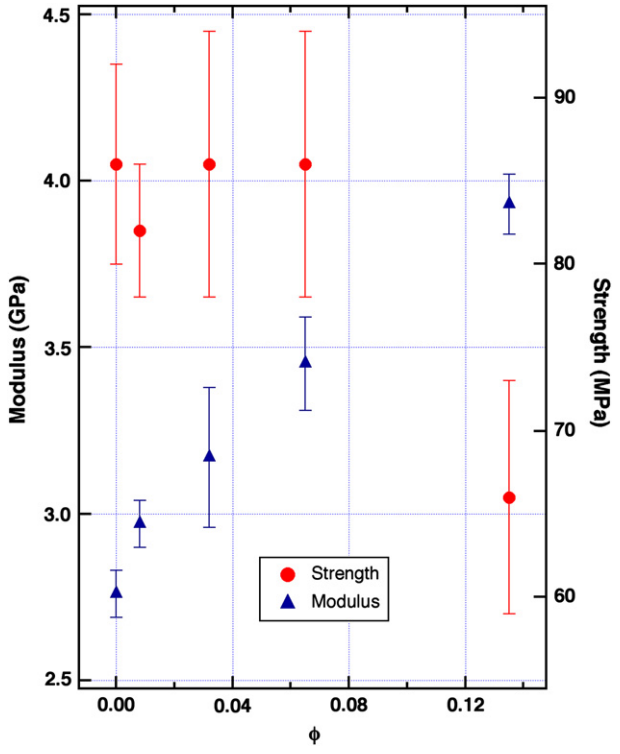

Fig. 8. Dependence of the tensile modulus and strength on SiO_2 loading.

Table 2
Summary of mechanical values presented in Figs. 8 and 11

SiO_2 loading		Modulus (GPa)		Strength (MPa)		Toughness (kPa m$^{-1/2}$)		Energy (J m^{-2})
wt%	ϕ	E	Dev	σ	Dev	K_{1C}	Dev	G_{1C}
0.00	0.000	2.76	0.07	86	6	1381	85	606
1.25	0.008	2.97	0.07	82	4	1838	131	998
5.00	0.032	3.17	0.21	86	8	1916	155	1016
10.00	0.065	3.45	0.14	86	8	1587	85	640
20.00	0.135	3.93	0.09	66	7	–	–	–

$$E_\delta = 1 + 2.5\phi. \tag{8}$$

This equation predicts a weaker dependence on volume fraction than that observed as shown in Fig. 9. To bring the Smallwood calculation into alignment with the experimental data, there are several adjustments that could be made. These include assuming that the silica particle is larger than determined from previous analysis, that the neat resin properties are altered by the presence of the silica, or that the silica particle with excluded volume acts as a core–shell particle with a specific effective modulus (discussed further in Section 4.2). To estimate the larger silica particle size, we have to assume that the effective volume fraction, $\phi_{\text{eff-mod}}$, is larger than the actual volume fraction, ϕ, of SiO_2:

$$E_\delta = 1 + 2.5\phi_{\text{eff-mod}} = 1 + 3.33\phi, \quad \phi_{\text{eff-mod}} = 1.33\phi. \tag{9}$$

The mechanically effective particle radius is

$$\xi_{\text{mech}} = 2R\left(\frac{\phi_{\text{eff-mod}}}{\phi}\right)^{1/3}. \tag{10}$$

For a nominal particle radius of 70 Å, $\xi_{\text{mech}} = 7$ Å. The resulting additional thickness of 7 Å is consistent with the larger particles

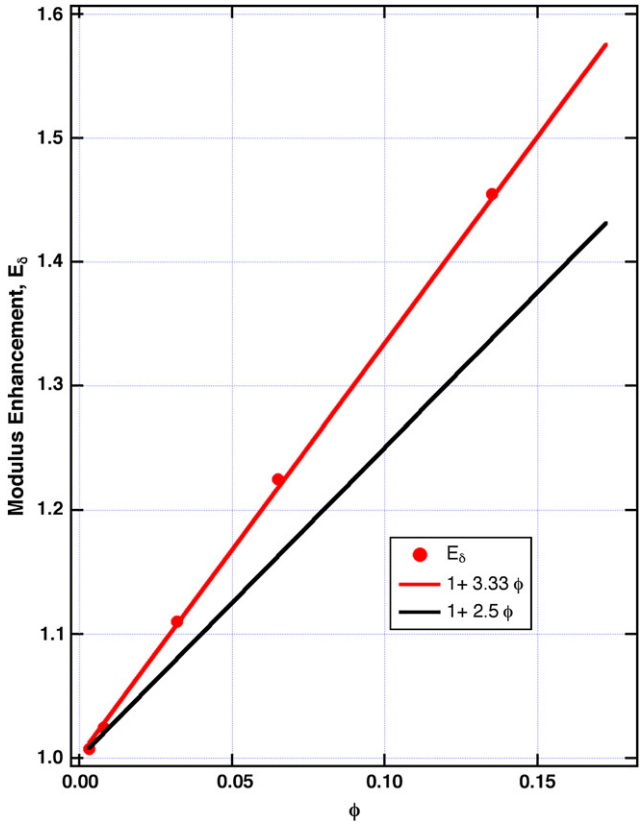

Fig. 9. Filler loading dependence of the modulus enhancement factor; ϕ is the volume fraction SiO_2.

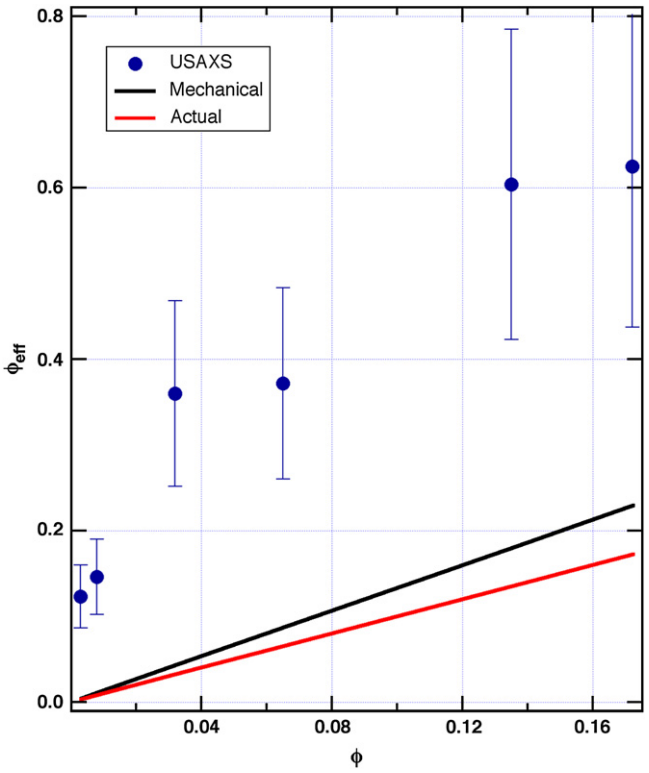

Fig. 10. Comparison of the packing factor measured by USAXS (Eq. (6)) with that predicted from the effective core–shell volume fraction calculated from Eq. (9). The actual volume fraction, ϕ, is calculated from the weight fraction loading and the densities of the filler and matrix. The plot shows that the mechanical properties are close to that predicted for highly dispersed rigid spheres; it also shows that the ordering observed by USAXS is not due to any mechanically significant shell around the particles.

radius values measured for individual samples, but inadequate to explain the strong correlations observed by USAXS and TEM. If one considers the packing parameter k, however, the 7-Å layer has a significant effect at high loading. Fig. 10 compares the effective volume fraction from USAXS (Eq. (6)) and modulus (Eq. (9)) to the actual volume fraction of SiO_2 based on weight fraction. The lack of agreement between the two techniques further demonstrates that the ordering observed by USAXS is not due to a increased silica particle size or equivalent mechanically significant shell around the particles.

The toughness of the unfilled Epon862/W and SiO_2/Epon862/W nanocomposites was measured by compact-tension testing. The fracture toughness as a function of loading is shown in Fig. 11. The filler increases the fracture toughness of the unfilled resin by as much as 30%, which is consistent with similar studies in the literature [17,18]. Due to the brittle nature of the 20 wt% sample, the toughness was not tested.

The fracture surface generated during the compact-tension test for both the unfilled resin and 1.3-wt% samples was examined by SEM (Fig. 12a and b). The images show increased roughness and plastic deformation in comparison to the smooth and featureless fracture surface of the unfilled Epon862/W. A summary of the modulus, strength, and toughness data is given in Table 2.

The observed decrease in fracture toughness (Fig. 11) above 5 wt% may be linked to a difference in resin properties – either a decrease in T_g or a decrease in coupling between the particles. The lower T_g may indicate that the regions of lower cross-link density provide low energy paths around the toughening particles. From the increase in surface area of the fracture surface with nanosilica and the change from a stepped surface to characteristic hackles, it

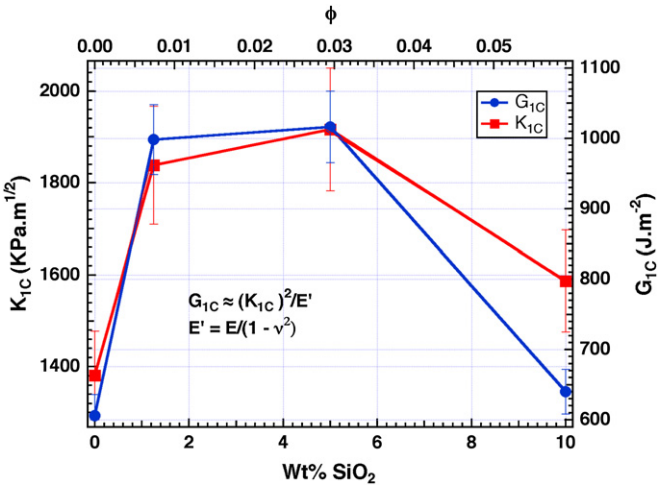

Fig. 11. Compact-tension results (fracture toughness and fracture energy) measured for four different SiO_2 (by weight): 0.0 (unfilled Epon862/W), 1.3, 5.0, and 10.0 wt%.

appears that several mechanisms including those previously mentioned may be operative.

4. Discussion

4.1. Thermal properties and morphological development

In a study of 100-nm diameter spherical SiO_2 in epoxy [22], Sun et al. concluded that a region of high polymer chain mobility exists in the presence of the nanosilica. These authors observed a decrease in T_g that was directly proportional to SiO_2 loading for samples above 10 wt% (approx. −1.3 °C/wt% SiO_2). The effect appeared to be size dependent because micron-sized SiO_2 showed no change in T_g at similar loadings. Other researchers attribute the decrease in T_g with nanosilica loading to the catalyzed reaction of epoxy with surface hydroxyl groups, which can lead to the formation of an amine rich shell around the nanoparticle and subsequent shifting of the epoxy/amine stoichiometry to induce higher cross-linking of the matrix [23]. The details of the effects of the Nissan nanosilica on kinetic constants of a different epoxy cure have also recently been investigated [24]. Still other researchers suggest that the compressive force due to the mismatch in coefficient of thermal expansion can aid in toughening at selected temperatures [25].

In the present study, we examined SiO_2 particles five times smaller than Sun et al. and found that samples beyond 5 wt% have a threefold larger decrease in T_g (approx. −3.8 °C/wt% SiO_2). It is not clear why this decrease is only found beyond a critical loading (5%). Furthermore, we observe a suppression of the cure temperature in direct proportion to the amount of SiO_2 added (−1.2 °C/wt% SiO_2 by rheological measurements and −1.6 °C/wt% SiO_2 by thermal measurements). This suppression in cure temperature was not observed for the larger 100-nm diameter particles.

Whether a region of enhanced free volume close to the nanoparticle surface or catalyzed reaction by surface hydroxyls exists, the cure temperature would be expected to decrease from the enhanced mobility or reaction rate. The fact that the overall curing reaction occurs at lower temperatures suggests that the active region is not "consumed" by the cross-linking reaction in the early stages of reaction. Instead, the effect persists within the curing resin to shift the temperature of maximum reaction rate (greatest slope). Though the active regions would not have sufficient contrast to be detected in the obtained scattering profiles, it is plausible that this effect contributes to the rheological separation of the SiO_2 particles by more than 10 times their particle diameter. The change

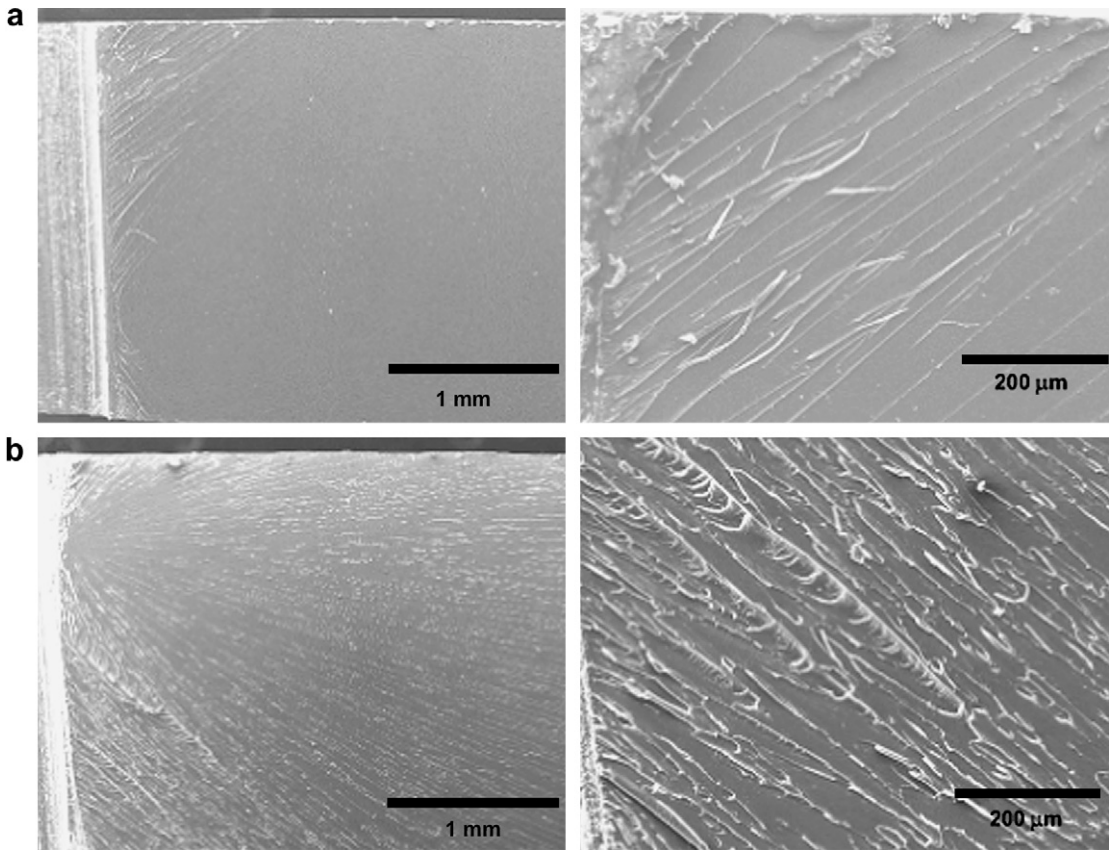

Fig. 12. Fracture surface of the (a) unfilled Epon862/W and (b) the composite filled with 1.3 wt% SiO_2.

in reaction kinetics and local stoichiometry can create corresponding changes in cross-link density. At very high particle loading, the potential exist for the transport of amine and epoxy molecules to be significantly impeded by the large number of particles. Thus, regions with very poor local stoichiometry and low cross-link density are created. This would result in a lower and possibly separate T_g [33]. However, since a single tan δ peak remains with no significant broadening as measured by DMA (Fig. 4), no evidence for large-scale phase separation or heterogeneity is apparent. Unless masked by an initially broad tan δ, the proportional decrease in T_g with loading above 5 wt% is either uniformly decreased in cross-link density or uniformly plasticized by the large volume fraction of high mobility regions. However, a corresponding decrease in modulus that normally accompanies plasticization and decreased cross-link density is not observed. Instead, the modulus is even greater than predicted by theory as is discussed below.

4.2. Effect of excluded regions on composite mechanical properties

As specifically discussed for nanosilica and epoxy by Johnsen et al. [34], the Lewis–Nielsen predictions for modulus [35] vary depending on the nature of the interface. However, predictions can be bound by assuming a perfect "no-slip" interface or a perfectly non-interacting "slip" interface. Fig. 13 displays the experimental modulus data compared to two ranges calculated using the Lewis–Nielsen theory [35]. These experimental data are not bound by the Lewis–Nielsen predictions for the "slip" and "no-slip" conditions if the predictions are based upon a neat resin modulus = 2.76 GPa.

To explain the deviations from the Lewis–Nielsen predictions and the previously mentioned Smallwood predictions, we considered two possibilities. First, the silica particles with the surrounding excluded volume behave as core–shell particles with a larger contribution to the overall nanocomposite modulus than predicted for the simple silica–epoxy system. To determine the effective modulus contribution of the silica particles and the excluded volume ($E_{c\ \phi\text{-excluded}}$) we used the rule of mixtures and the values in Table 3:

$$E_{c\,\phi\text{-excluded}} = \frac{E_c - E_m + E_m\left(\phi_{\text{eff-USAXS}}\right)}{\phi_{\text{eff-USAXS}}} \tag{11}$$

However, based upon this calculation, we find the values for $E_{c\ \phi\text{-excluded}}$ to be inconsistent as a function of loading (Table 3). Thus, the lack of agreement between the experimental data and the Lewis–Nielsen model cannot be simply explained by a core–shell particle within an unaltered epoxy matrix.

The second possibility for the disagreement is that the SiO_2 particles alter the curing reaction throughout the sample volume, thus the modulus of the entire matrix is affected. To bring experimental data and the Lewis–Nielsen predictions into alignment, the value of composite modulus E_c under the condition of "no-slip" at the filler/matrix interface was adjusted by changing the Epon862/W modulus (E_m) in the Lewis–Nielsen model:

$$E_c = \frac{1 + (k_E - 1)\beta\phi}{1 - \beta\mu\phi}E_m \tag{12}$$

where k_E is the generalized Einstein coefficient equal to 2.5 (under the "no-slip" condition), and β and μ are values specific to the moduli of the system constituents and filler concentration ϕ, respectively [31,32]. The application of Eq. (12) also included the assumption of no agglomeration among the filler particles. By adjusting E_m in Eq. (12) such that E_c matches our measured values ($E_{c\ \text{experimental}}$), we can determine an adjusted value for the matrix

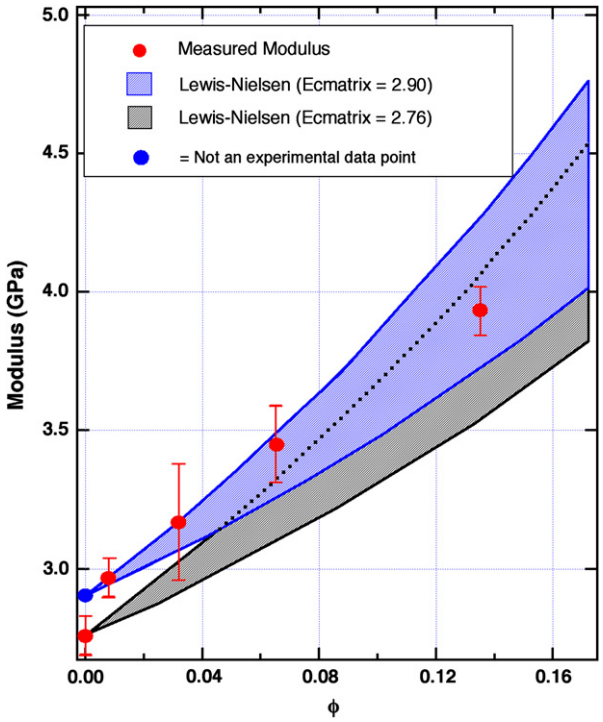

Fig. 13. Measured moduli data from Table 3 compared to two cases for the Lewis–Nielsen "slip" and "no slip" predictions. The measured values are higher than predicted by the model when the neat-matrix (0% SiO_2) modulus $E_{c\ matrix} = 2.76$. However, by increasing the neat matrix modulus to $E_{c\ matrix} = 2.90$ (blue circle), the experimental data are bound by the model predictions. This observation suggests the presence of the SiO_2 particles increases the modulus of all of the matrix resin (not just the resin in the observed exclusion zone).

($E_{c\ matrix}$). The values for $E_{c\ matrix}$ (Table 3) are very reasonable, leading us to the conclusion that the entire matrix of the composite samples is altered due to the presence of the SiO_2. Fig. 13 shows the result of increasing the modulus value of neat epoxy ($E_{c\ matrix}$) from 2.76 to 2.90. With this change, the experimental results are then bounded by the Lewis–Nielsen model. Furthermore, by using the modified value $E_{c\ matrix} = 2.90$, the slope of the fit (red line) in Fig. 9 would shift from 3.33 to 2.70, which more closely agrees with value of 2.5 predicted by Smallwood (Eq. 8).

As discussed previously, there are many reported mechanisms for the improvement in fracture toughness in epoxy resins. Following the approach of Johnsen et al., we can also rule out several possible mechanisms [34]. First, a crack opening displacement of 12 μm can be calculated for the neat resin undergoing a crack pinning mechanism. Since this mechanism requires the particles to be larger than this displacement, it is doubtful that our 12-nm SiO_2 particles use this mechanism. Similarly, given the length scale difference between the nanoparticles and the crack dimensions and the uniform dispersion, it is unlikely that incremental difference in toughness from the addition of nanosilica is caused by a crack deflection mechanism. Further, because the T_g decreases with SiO_2 loading, polymer immobilization can also be ruled out. The mechanism of void formation might be present as has been previously described for a similar system. However, this possibility could not be conclusively confirmed due to the small dimensions of the particles involved.

From Fig. 12a and b, the fracture surface micrographs are characterized by enhanced plastic deformation in the tougher samples as would be expected in crack deflection. However, the high concentration of deformation lines at 45° to the crack propagation direction suggests that shear banding is a dominant energy absorption mechanism. It has been previously reported that silicate nanoparticles, which generate local regions of high mobility/low cross-link density in epoxy, can initiate shear banding at lower loads [36,37]. From our analysis, enhanced shear banding is the most viable mechanism for energy absorption.

Table 3
Calculated values for the moduli of the excluded volume surrounding the SiO_2 particles

wt%	ϕ	$\phi_{eff\text{-}USAXS}$	ϕ_{matrix}	$E_{c\ experimental}$	$E_{c\ \phi\text{-}excluded}$*	$E_{c\ matrix}$*
1.25	0.008	0.146	0.854	2.97	4.20	2.91
5.00	0.032	0.360	0.640	3.17	3.90	2.90
10.00	0.065	0.372	0.628	3.45	4.62	2.87
20.00	0.135	0.604	0.396	3.93	4.69	2.67

The calculated values for $E_{c\ \phi\text{-excluded}}$ (Eq. 11) are higher than any other values in the literature known to us for an Epon862/W system, thus one possibility for the deviation from the model data is an increased modulus of the entire matrix resulting from the presence of the SiO_2 particles. The $E_{c\ matrix}$ values were determined with Eq. 12 by adjusting the matrix modulus (E_m) in the Lewis–Nielsen model (for the "no-slip condition") such that E_c would agree with the measured values for $E_{c\ experimental}$ at a given value of ϕ.

* Calculated values ($E_{c\ \phi\text{-excluded}}$ using Eq. 11, $E_{c\ matrix}$ using Eq. 12)

5. Conclusions

This work presents the characterization of a system of SiO_2/epoxy nanocomposites that shows toughness and modulus improvements without sacrificing the working temperature of the resin. Thermal and rheological studies indicated (1) the processing scheme is effective for creating SiO_2/epoxy nanocomposites with intriguing properties, and (2) the nanosilica particles induce an exclusion zone that lowers the reaction temperature and can also lower T_g of the nanocomposite at high-filler loadings. Microscopy and scattering reveal excellent dispersion with minimal aggregation with loadings up to 25 wt%. Mechanical testing demonstrates a 30% enhancement in toughness at lower loadings and a modulus increase that was bounded by Lewis–Nielson prediction for an interface with and without slip when an enhanced modulus for the neat epoxy was assumed. Concerning modulus enhancement, the exclusion zone is independent of loading.

The morphology determined by USAXS is consistent with an exclusion zone extending up to 10 times the core radius. There is no evidence of formation of a filler network for loadings up to 25 wt%, which is approximately the percolation threshold for the silica particles and substantially above the percolation threshold for the exclusion zone.

These results indicate that the nanoparticles are individually dispersed, and the dispersed SiO_2 colloids are effective reinforcing agents for hard resins. Because of the improved mechanical properties, the low viscosity processing, and the excellent dispersion, this approach appears promising for use in the manufacturing of advanced reinforced composites.

Acknowledgements

The authors thank Prashant Rajan (University of Cincinnati, Cincinnati, OH) and Dr. Doug Kohls (University of Cincinnati, Cincinnati, OH) for collecting the dynamic light scattering data shown in Fig. 1b. We also thank Dr. Jan Ilavsky (Advanced Photon Source) for his assistance in collecting and analyzing the USAXS data presented in this work. The USAXS data were collected on the X-ray Operations and Research beam line 32-ID-B at the Advanced Photon Source, Argonne National Laboratory (Argonne, IL). The use of the Advanced Photon Source is supported by the U. S. Department of Energy, Office of Science, Office of Basic Energy Sciences, under Contract No. W-31-109-ENG-38.

The authors would also like to thank Dr. Peter Mirau (Air Force Research Laboratory, Wright Patterson Air Force Base, Dayton, OH) for his contribution to the collection and analysis of the NMR data,

and Mr. Ron Esterline (University of Dayton Research Institute, Dayton, OH) for his assistance in sample preparation and collection of the mechanical data. This work is supported by the Air Force Office of Scientific Research and Air Force Research Laboratory, Materials & Manufacturing Directorate, Contract No. FA8650-05-D-5052.

References

[1] Ellis B. Chemistry and technology of epoxy resins. New York, NY: Blackie Academic & Professional; 1993.
[2] Wetzel B, Rosso P, Haupert F, Friedrich K. Epoxy nanocomposites – fracture and toughening mechanisms. Engineering Fracture Mechanics 2006;73: 2375–98.
[3] Bagheri R, Pearson RA. Role of particle cavitation in rubber-toughened epoxies. 1. Microvoid toughening. Polymer 1996;37:4529–38.
[4] Bucknall CB, Lazzeri A. Rubber toughening of plastics – part XIII – dilatational yielding in PA6.6/EPR blends. Journal of Materials Science 2000;35:427–35.
[5] Lazzeri A, Bucknall CB. Dilatational bands in rubber-toughened polymers. Journal of Materials Science 1993;28:6799–808.
[6] Sultan JN, McGarry FJ. Effect of rubber particle size on deformation mechanisms in glassy epoxy. Polymer Engineering and Science 1973;13:29–34.
[7] Cardwell BJ, Yee AF. Toughening of epoxies through thermoplastic crack bridging. Journal of Materials Science 1998;33:5473–84.
[8] Singh RP, Zhang M, Chan D. Toughening of a brittle thermosetting polymer: effects of reinforcement particle size and volume fraction. Journal of Materials Science 2002;37:781–8.
[9] Faber KT, Evans AG. Crack deflection processes. 1. Theory. Acta Metallurgica 1983;31:565–76.
[10] Evans AG, Faber KT. Crack-growth resistance of microcracking brittle materials. Journal of the American Ceramic Society 1984;67:255–60.
[11] Lee J, Yee AF. Inorganic particle toughening II: toughening mechanisms of glass bead filled epoxies. Polymer 2001;42:589–97.
[12] Kinloch AJ, Mohammed RD, Taylor AC, Eger C, Sprenger S, Egan D. The effect of silica nano particles and rubber particles on the toughness of multiphase thermosetting epoxy polymers. Journal of Materials Science 2005;40:5083–6.
[13] Han JT, Cho K. Layered silicate-induced enhancement of fracture toughness of epoxy molding compounds over a wide temperature range. Macromolecular Materials and Engineering 2005;290:1184–91.
[14] Han JT, Cho K. Nanoparticle-induced enhancement in fracture toughness of highly loaded epoxy composites over a wide temperature range. Journal of Materials Science 2006;41:4239–45.
[15] Kinloch AJ, Taylor AC. The mechanical properties and fracture behaviour of epoxy–inorganic micro- and nano-composites. Journal of Materials Science 2006;41:3271–97.
[16] Ragosta G, Abbate M, Musto P, Scarinzi G, Mascia L. Epoxy–silica particulate nanocomposites: chemical interactions, reinforcement and fracture toughness. Polymer 2005;46:10506–16.
[17] Rosso P, Ye L, Friedrich K, Sprenger S. A toughened epoxy resin by silica nanoparticle reinforcement. Journal of Applied Polymer Science 2006;100: 1849–55.
[18] Zhang H, Zhang Z, Friedrich K, Eger C. Property improvements of in situ epoxy nanocomposites with reduced interparticle distance at high nanosilica content. Acta Materialia 2006;54:1833–42.
[19] Wetzel B, Haupert F, Friedrich K, Zhang MQ, Rong MZ. Impact and wear resistance of polymer nanocomposites at low filler content. Polymer Engineering and Science 2002;42:1919–27.
[20] Laine RM, Choi JW, Lee I. Organic–inorganic nanocomposites with completely defined interfacial interactions. Advanced Materials 2001;13:800–3.
[21] Bugnicourt E, Galy J, Gerard JF, Barthel H. Effect of sub-micron silica fillers on the mechanical performances of epoxy-based composites. Polymer 2007;48: 1596–605.
[22] Sun YY, Zhang ZQ, Moon KS, Wong CP. Glass transition and relaxation behavior of epoxy nanocomposites. Journal of Polymer Science, Part B: Polymer Physics 2004;42:3849–58.
[23] Rosso P, Ye L. Epoxy/silica nanocomposites: nanoparticle-induced cure kinetics and microstructure. Macromolecular Rapid Communications 2007; 28:121–6.
[24] Ghaemy M, Amini Nasab SM, Barghamadi M. Preparation and nonisothermal cure kinetics of DGEBA–nanosilica particle composites. Polymer Composites 2008;29:165–72.
[25] Deng S, Ye L, Friedrich K. Fracture behaviours of epoxy nanocomposites with nano-silica at low and elevated temperatures. Journal of Materials Science 2007;42:2766–74.
[26] Hussain M, Nakahira A, Nishijima S, Niihara K. Fracture behavior and fracture toughness of particulate filled epoxy composites. Materials Letters 1996;27: 21–5.
[27] Chen CG, Curliss D. Resin matrix composites: organoclay–aerospace epoxy nanocomposites, part II. SAMPE Journal 2001;37:11–8.
[28] Koppel DE. Analysis of macromolecular polydispersity in intensity correlation spectroscopy: the method of cumulants. The Journal of Chemical Physics 1972; 57:4814–20.
[29] Beaucage G, Schaefer DW. Structural studies of complex-systems using small-angle scattering – a unified Guinier power-law approach. Journal of Non-Crystalline Solids 1994;172:797–805.
[30] Guinier A, Fournet G. Small-angle scattering of X-rays. New York, NY: John Wiley and Sons, Inc.; 1955.
[31] Roe RJ. Methods of X-ray and neutron scattering in polymer science. New York: Oxford University Press; 2000.
[32] Beaucage G. Approximations leading to a unified exponential power-law approach to small-angle scattering. Journal of Applied Crystallography 1995; 28:717–28.
[33] Liu YL, Hsu CY, Wei WL, Jeng RJ. Preparation and thermal properties of epoxy–silica nanocomposites from nanoscale colloidal silica. Polymer 2003; 44:5159–67.
[34] Johnsen BB, Kinloch AJ, Mohammed RD, Taylor AC, Sprenger S. Toughening mechanisms of nanoparticle-modified epoxy polymers. Polymer 2007;48: 530–41.
[35] Nielsen LE, Landel RF. Mechanical properties of polymers and composites. New York, NY: M. Dekker; 1994.
[36] Akbari B, Bagheri R. Deformation mechanism of epoxy/clay nanocomposite. European Polymer Journal 2007;43:782–8.
[37] Garg AC, Mai YW. Failure mechanisms in toughened epoxy-resins – a review. Composites Science and Technology 1988;31:179–223.